Applied Physics A (2020)126:56
https://doi.org/10.1007/s00339-019-3234-0

Applied Physics A
Materials Science & Processing

Experimental and computational perspectives on linear and non-linear optical parameters of an orthorhombic crystal for optical limiting applications

Sarath Ravi[1] · Rakhi Sreedharan[1] · K. R. Raghi[2,3] · T. K. Manoj Kumar[2,3] · K. Naseema[4]

Received: 20 October 2019 / Accepted: 13 December 2019

Abstract

4-Dimethylaminopyridinium 3,5-dinitrobenzoate (DMAPDNBA), a charge transfer complex, was synthesized and successfully grown by slow evaporation solution growth technique. Single-crystal X-ray diffractogram reveals that the material crystallizes in orthorhombic system with non-centrosymmetric space group $P2_12_12_1$ with cell parameters $a = 5.92$ Å, $b = 13.77$ Å, $c = 18.64$ Å, and $V = 1519$ Å^3. Powder XRD and FTIR spectral investigation were carried out to analyse the crystallinity of the material and for assigning vibrations to identify the different functional groups existing within the material. The optical transmittance in the visible and near IR (400–800 nm) regions with lower cutoff wavelength of 227 nm, luminescence spectrum, and the optical band gap of 5.45 eV sufficiently fulfilled the requirement for non-linear optical applications. The thermal exploration analysis (TG–DSC) confirmed the stable nature of the compound up to 190 °C, and dielectric constant measurement of the obtained sample enhanced the property of non-linear optical activity at higher frequencies. The mechanical property of DMAPDNBA was evaluated using Vickers's hardness test which confirmed that the material belonged to the soft category. The frequency conversion efficiency of the grown sample was measured to be eightfold that of the reference potassium dihydrogen phosphate, which exploits the potentiality of the charge transfer complex to be used as a promising candidate for various laser-assisted NLO applications. Third-order non-linearity was measured adopting Z-Scan technique, and the optical limiting/switching efficiency of the complex was verified with the optical limiting threshold value of 10.64 J/cm^2 and figure of merit property, confirming the capability of the material for switching applications. The threshold value of laser damage was found to be 1.74 GW/cm^2. Theoretical investigations were performed using density functional theory (DFT-B3LYP) approach to estimate and predict various linear and non-linear optical properties of the DMAPDNBA complex. The first-order hyperpolarizability value of the DMAPDNBA molecule was found to be 19 times that of the standard organic crystal, urea. In short, all the above findings designate the candidature of the charge transfer complex, DMAPDNBA, for photonic applications.

Keywords Organic NLO crystal · Crystal growth · Linear optical properties · Non-linear optical studies · Optical limiting · Quantum chemistry calculations

1 Introduction

Nowadays, the potential use of high-power laser systems in photonics field has urged solid-state researchers in need of non-linear optical materials. Indeed, such materials have attained much attention due to their significant uses in the field of photonics such as frequency conversion, electro-optical switches, optical storage system and optical information processing [1, 2]. The selection of crystalline material can be correlated with the physicochemical properties such as molecular non-linearity, transparency, thermal–mechanical stability and frequency generation capability. Various

✉ K. Naseema
nascsarath@gmail.com

[1] School of Pure and Applied Physics, Payyanur Campus, Kannur University, Kannur, Kerala 670327, India

[2] School of Chemical Sciences, Payyanur Campus, Kannur University, Kannur, Kerala 670327, India

[3] Indian Institute of Information Technology and Management, Trivandrum, Kerala 695581, India

[4] Department of Physics, Nehru Arts and Science College, Kanhangad, Kerala 671314, India

Published online: 21 December 2019

categories of materials such as organic/inorganic oxides, organometallic compounds, semiconductors and conjugated polymers exhibiting good non-linear optical characteristics have been reported [3, 4]. Recently, organic non-linear optical (NLO) systems have gained wide exposure due to the promising NLO response and higher stability reflecting their suitability in second harmonic generations, optical parametric oscillations and electro-optic modulation. It is evident that the high non-linearity of the organic compounds arises due to the delocalization of the electronic structure in π-conjugated state with the appearance of electron-accepting and -donating clusters on the either side of the system and asymmetries in the π electron system which makes it a highly polarizable entity demanded by most of the NLO applications [1, 5, 6]. The concept of charge transfer (CT) interactions originated by the exchange of charge between donor and acceptor groups and the resulting intermolecular hydrogen bonding (N^+–H…O^-) were first presented by Mullikan and it seems to be a most challenging interaction in the field of photonics [7–9].

In the recent decade, pyridine and its derivatives play a dominant role in technological fields, since they are used as solvents and starting material for the synthesis of target compounds such as insecticides, herbicides, medicines, vitamins, food flavourings, feed additives, dyes, rubber chemicals, explosives, disinfectants and adhesives. One of the outstanding pyridine compounds capable of executing unbeatable CT process is found to be 4-dimethylaminopyridine (DMAP), and crystal structure and properties of various such salts of DMAP have been reported in the earlier literature [10–17]. Moreover, it is an acylation catalyst used in the synthesis of agrochemicals and pharmaceuticals [18, 19]. On the other hand, dinitrobenzoate compounds are of great interest because of their biological activities. Among them, 3,5-dinitrobenzoic acid is a potential candidate with drastic anti-creatinine properties and an effective reagent in radiation treatments. Some synthetic dinitrobenzoic compounds have shown useful properties in DNA and oligosaccharide [20, 21]. Besides the promising use of pyridine derivatives and dinitrobenzoate compounds for biological applications, the significance of those derivatives for photonic applications remains unexplored. 4-Dimethylaminopyridinium compounds linked with other aromatic rings of an organic nature have been realized as an imperative tool in the second harmonic generation (SHG) process, due to the absence of phase transition and the challenging physio-chemical properties [22–25]. Hence, the present study deals with the investigation of the non-linear behaviour of a pyridine co-related benzoic acid compound under various experimental and theoretical characteristic properties.

In the attempts of growing new potential crystals for device fabrication, in the present study we have grown a new crystal 4-dimethylaminopyridinium 3,5-dinitrobenzoate (DMAPDNBA) by a slow evaporation solution growth technique in which the charge transfer takes place between 4-dimethylaminopyridine and 3,5-dinitrobenzoic acid which paves the way for the formation of an organic non-centrosymmetric charge transfer complex. Here the OH group in the 3,5dinitrobenzoic acid has protonated the nitrogen of 4-dimethylamino pyridine, i.e. a proton in the donor group is transferred to the base and bonded together to form an intermediate compound. On the basis of this, the growth, structural elucidation, electrical, thermal, mechanical and non-linear studies of the mixed crystal DMAPDNBA are

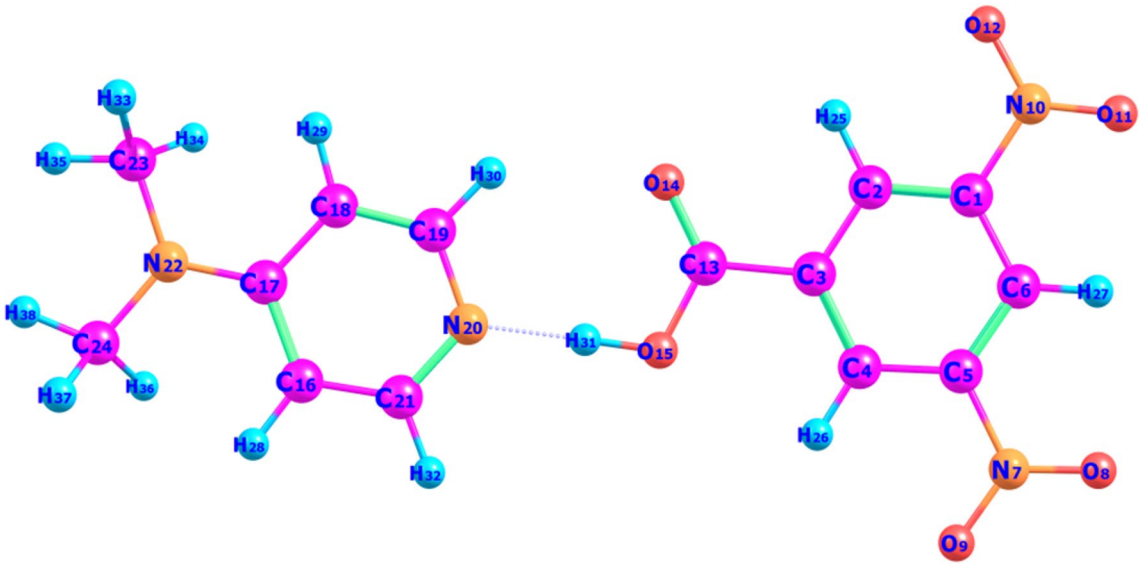

Fig. 1 2D molecular structure of DMAPDNBA

discussed in detail along with the quantum computational background employing density functional theory (DFT) using the 2D optimized geometry of the compound (Fig. 1).

2 Experimental procedure

2.1 Material synthesis

The title compound was synthesized by taking equimolar ratio of 4-dimethylamino pyridine (DMAP) and 3,5-dinitrobenzoic acid (DNBA) in ethanol. The saturated solution of the mixture was prepared and stirred vigorously about 6 h and the resultant yellow coloured solution was filtered off using Whatman filter paper and placed in a dust-free atmosphere for slow evaporation. Small yellow colour needle-shaped seed crystals of 4-dimethylamino pyridinium-3,5-dinitrobenzoate (DMAPDNBA), suitable for single-crystal XRD was observed within a week.

The reaction mechanism involved is as follows:

$$C_7H_{10}N_2 + C_7H_4O_6N_2 \rightarrow C_7H_{11}N_2^+C_7H_3O_6N_2^-.$$

2.2 Solubility of the material

Good quality optical crystals can only be obtained under an optimized growth process. The optimization criteria can be achieved by analysing the solubility of the material under a suitable solvent. To get the solubility data, initially a bulk amount of the compound was synthesized and stored in the crushed form. A small amount of the prepared compound was dissolved in 100 ml of water at 30 °C by consequent stirring employing a constant temperature bath with a temperature accuracy of about ± 0.01 °C and about 5 ml of the clear solution was pipetted out into a Petri dish of known weight. The solubility of the material in 5 ml of water was then determined gravimetrically by allowing the solvent to evaporate completely to weigh the mass of the remaining solute. The process was repeated at 30 °C with ethanol as the solvent. The solubility curve was plotted for the material with water and ethanol as a function of different temperatures ranging from 30 to 50 °C as in Fig. 2.a. The depicted figure reveals that the material holds positive temperature coefficient, since the solubility of the material increases with increase in temperature. But for the growth procedure, ethanol was chosen to be the appropriate solvent because the solubility of the material in water lags from the solubility in ethanol by a large quantity.

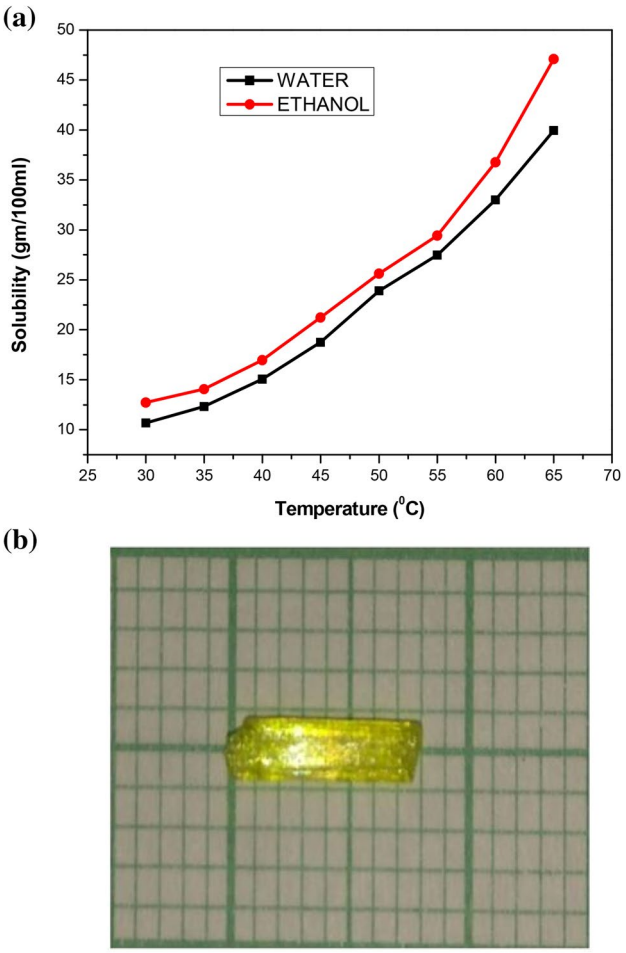

Fig. 2 **a** Solubility curve of DMAPDNBA crystal, **b** as-grown single crystals of DMAPDNBA

2.3 Crystal growth

The supersaturated solution of DMAPDNBA compound was prepared in accordance with the solubility data (10 g/100 ml) in ethanol at 30 °C. The obtained solution was filtered and covered off with perforated polythene cover and placed in a vibration-free atmosphere for slow evaporation at room temperature to initiate the nucleation process. The first speck of nucleation was observed within 2 days and yellow-coloured single crystals of significant dimension were harvested in about 15 days from the mother solution. To obtain superior quality crystals of the required dimension, single crystals of DMAPDNBA were further purified by consecutive recrystallization with acetone and crystals of dimension (8*2*1) mm^3 were harvested within few days. The grown crystal of DMAPDNBA is as shown in Fig. 2b.

2.4 Characterization techniques

Single-crystal X-ray diffraction (SXRD) studies were carried out using ENRAF–NONIUS CAD4 diffractometer software for evaluating the structure and cell parameters of the formed charge transfer complex. Powder X-ray diffraction (PXRD) pattern was obtained using Cary 630 with ATR-Agilent technologies to determine the purity and crystallinity of the obtained DMAPDNBA complex. Fourier transform infrared spectrum (FTIR) was observed through Rigaku Miniflex 600 setup for confirming the various vibrations corresponding to the functional groups present in the material. Thermogravimetric and differential scanning calorimetric (TG&DSC) curves were obtained via the NETZSCH STA 449F5 STA449FSA-0231-M thermal analysis system to examine the thermal stability of the complex. UV–Vis–NIR spectrum and emission spectrum recorded by Varian Carry 5000 spectrophotometer and Shimadzu Spectrofluorophotometer to confirm the translucence and fluorescence behaviour of the obtained intermediate compound. LEITZ WETZLER microhardness tester with diamond pyramidal indenter was used to establish the mechanical stability of the material and Kurtz Perry powder technique was employed to confirm the non-linearity of the non-centrosymmetric complex. Dielectric measurements were executed by HIOKI 3532 LCR HITESTER arrangement and the Z-Scan setup was exploited for determining third-order non-linear parameters of the sample.

2.5 Quantum computational calculations

Theoretical approach facilitates the ground state optimization of molecular geometry for estimating the chemical reactivity of the molecule by frontier molecular orbital analysis, electrostatic potential effects through a three-dimensional electrostatic potential plot and the NLO activity of the system with the electronic properties such as dipole moment, polarizability and hyperpolarizability. In the present scenario, the conventional hybrid DFT functionals and ab initio HF level of theory was utilized under 6-31G*d(p) basis set with Gaussian 09 program package as the mathematical tool for establishing the computational details of the title compound, DMAPDNBA.

3 Results and discussion

3.1 Crystallographic studies

The grown crystals of the charge transfer complex, DMAPDNBA was subjected to single-crystal XRD to determine the unit cell parameters, crystal structure and the space group. The obtained XRD data were further analysed using ENRAF–NONIUS CAD-4 diffractometer to compare those parameters with that of the reported literature [26] as shown in Table 1. It was thus confirmed that the crystal crystallizes in the orthorhombic system with $P2_12_12_1$ as the non-centrosymmetric space group.

Table 1 Comparative study of the cell parameters and structural data with the reported literature

Crystal data	Present study	Reported [26]
a (Å)	5.92	5.89
b (Å)	13.77	13.77
c (Å)	18.64	18.62
α (°)	90.00	90.00
β (°)	90.00	90.00
Υ (°)	90.00	90.00
Cell volume ((Å)^3)	1519.0	1509.7
Crystal system	Orthorhombic	Orthorhombic
Space group	$P2_12_12_1$	$P2_12_12_1$

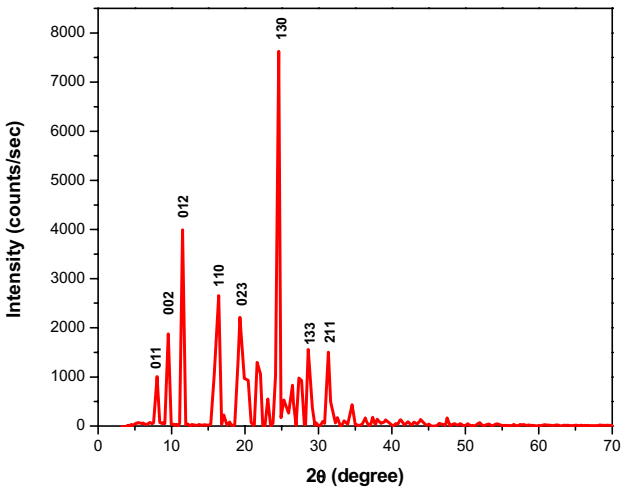

Fig. 3 Powder XRD pattern of the DMAPDNBA complex

Powdered sample of DMAPDNBA was scanned over an angular range of 0° to 70° in steps of 0.02° for a time interval of 2 s to determine the crystallinity and the purity of the grown complex. The analysis was performed using CuKα ($\lambda = 1.5148$ Å) radiation and the sharp specks corresponding to each 2θ angle illustrated in Fig. 3 confirm the crystalline nature of the complex thus obtained. The possible reflections can be found out using the relation (Eq. 1) connecting interplanar spacing (d) and the Miller indices (hkl) for the orthorhombic crystal system.

$$\frac{1}{d^2} = \left[\frac{h^2}{a^2} + \frac{k^2}{b^2} + \frac{l^2}{c^2}\right]. \quad (1)$$

Powder X-ray diffraction data of DMAPDNBA enables us to understand the crystalline behaviour of the grown crystal

by verifying various features such as crystallite size of the material, degree of crystallinity embedded within the grown crystal, dislocation density and the microstrain effect of the DMAPDNBA crystal.

The crystallite size of DMAPDNBA was determined using Debye–Scherrer's relation:

$$D = \frac{k\lambda}{\beta \cos\theta}, \tag{2}$$

where $k = 0.9$, $\lambda = 1.5405$ Å and β reflects the full width at half maximum (FWHM) value. The maximum peak intensity was found to be at the glancing angle, $2\theta = 21.029°$, and correspondingly the size of DMAPDNBA crystal was estimated to be 142 Å. The obtained value was then confirmed from the Hall Williamson plot and found to be in close agreement with Debye–Scherrer's findings. The dislocation density of DMAPDNBA crystal lattice was obtained from the equation:

$$\delta = \frac{1}{D^2}. \tag{3}$$

The occurence of strain within the lattice was observed and calculated from the Hall Williamson relation as follows:

$$\varepsilon = \frac{1}{\sin\theta}\left[\beta\cos\theta - \frac{\lambda}{D}\right]. \tag{4}$$

The determined value exactly matches with the slope of the linear fitted region of the plot with $\beta\cos\theta$ versus $\sin\theta$ (Figure 4). The percentage of crystallinity of the grown DMAPDNBA crystal was also evaluated and noticed to be 43%. The above said crystallographic parameters designate the sample as a typical crystal towards non-linear optical applications. The structural parameters of DMAPDNBA crystal are exhibited in Table 2.

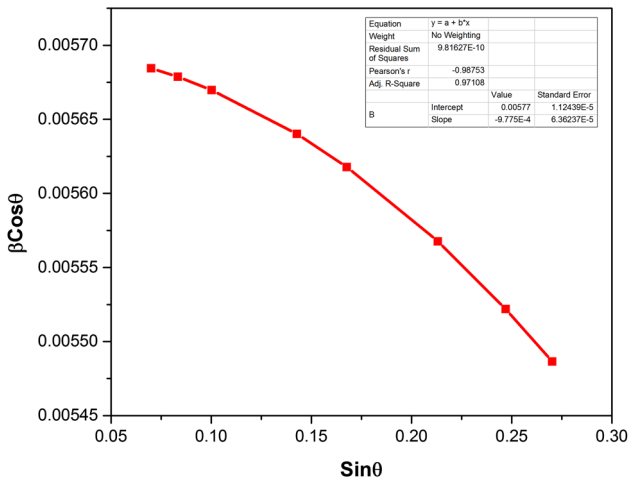

Fig. 4 Hall–Williamson plot with $\beta\cos\theta$ versus $\sin\theta$

Table 2 Structural parameters of the DMAPDNBA crystal

Crystallographic parameters	Values
Maximum peak	(2θ) 24.61°
FWHM (β)	0.33 (°)
Crystallite size	Debye–Scherrer equation: 243 Å
	Hall–Williamson plot: 173 Å
Dislocation density (δ)	$0.17*10^{12}$ g/cm^3
Microstrain (ε)	Hall–Williamson equation: −0.003
	Hall–Williamson plot: −0.002
Degree of crystallinity	64%

3.2 FTIR analysis

The FTIR spectrum of the charge transfer complex was recorded using Rigaku Miniflex 600 spectrophotometer in the frequency range of 4500 to 500 cm^{-1}. It is based on the principle that the molecules within the material absorb certain IR radiations corresponding to the frequencies required for executing vibrations and pave the way for a change in the net dipole moment exhibited by the absorption bands [27]. The IR spectrum obtained (Fig. 5) for the CT complex was then compared with that of the donor and acceptor spectra to confirm the formation of the newly charged complex. The methyl and hydroxyl groups in the spectrum act as the electron-donating groups, whereas the C–N groups on the pyridine ring and nitro groups act as the electron-accepting groups. Hence, the introduction of specific functional groups at the reactive active sites of 4-dimethylaminopyridinium 3,5-dinitrobenzoate (DMAPDNBA) reduces the π–π intermolecular stacking of molecule. The formation of electron push–pull structure enhances the intermolecular charge transfer mechanism, which decreases the band gap energy of the DMAPDNBA molecule and thereby provides better NLO responses (Table 3).

3.3 Thermal studies

Thermal analysis is a technique which helps us to study about the thermal stability of a material by analysing the change of the state of the obtained compound as a function of temperature. Here, the samples of DMAPDNBA were taken in an Al_2O_3 crucible with a microprocessor-aided temperature control setup and the analysis were carried out within the ambient temperature 500 °C at a heating rate of 10 °C in the nitrogen flux and the profile is exhibited in Fig. 6. From the thermogravimetric (TG) curve, the absence of endothermic or exothermic peaks below 190 °C shows a clear elucidation of the stability of the compound without any change of state before melting and it can be confirmed that the sample is free from physically adsorbed water. This higher range of stability reveals the purity as well as the

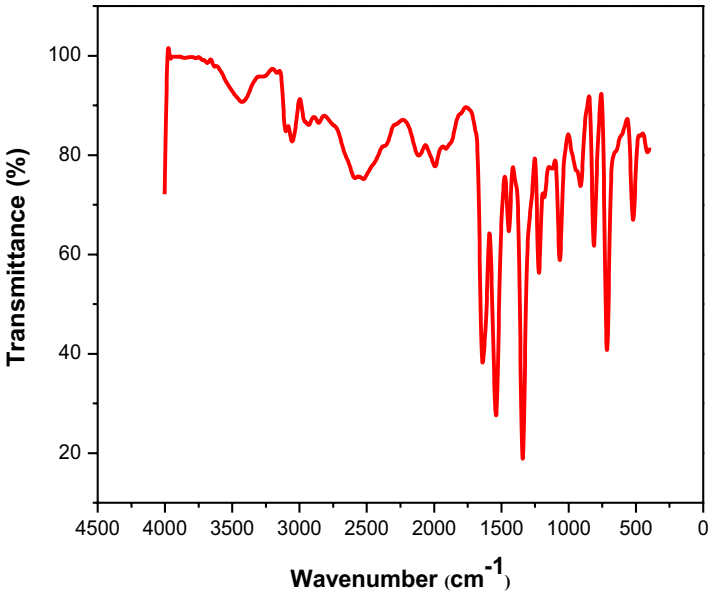

Fig. 5 FTIR spectrum of the DMAPDNBA complex

Table 3 Vibrational assignments of various functional groups of the DMAPDNBA complex

Wavenumber (cm^{-1})	Tentative assignments
3428	Characteristics of OH stretching vibration
3096	Aromatic C–H stretching of nitrogen heterocyclic compounds
3043	CH_3 asymmetric stretching mode
2590, 2520	Symmetric and asymmetric stretching vibration of the CH_3 group
2110	Combination band of the aromatic ring
1988	C=O stretching vibration
1630	C–C stretching, plane bending of N–C–H and stretching of C–N in pyridine rings
1533	Stretching of N–C, plane bending of N–C–H, stretching of C–C and plane bending of C–H in pyridine rings
1438	O–H in plane bending mode
1342	C–C stretching mode coupled with C–H in plane bending mode
1220	N-$(CH_3)_2$ stretching vibrations with a coupling of Ph_2 ring C–C stretching modes
1054, 905	CH_3 rocking mode of methyl group
801	NO_2 scissoring when conjugated to C–C or aromatic molecules
713	Wagging mode of NO_2 group
512	Rocking mode of NO_2 group and asymmetric deformation of phenyl ring

perfection of the compound. The thermogram exhibits a single-stage weight loss after the melting point (190 °C) up to 338 °C which reflects the decomposition of the crystal into smaller fragments by the evolution of the volatile substances such as CO_2, CO, NO_2 and NH_3. The differential scanning calorimetric (DSC) study reveals that the sharp endothermic peak at 191.71 °C confirms the melting point of the complex with that of the TG curve, proving the superior quality and crystallinity of the synthesized sample, whereas the broad endothermic peak at 332 °C holds the complete decomposition of the material leaving the residue. It can therefore be concluded from the thermal analysis that the lattice forces are much stronger than the bonding forces, which moulds the material to be stable enough to withstand the changes due to thermal energy and results in a higher protonation between the donor and acceptor groups [28].

3.4 UV–VIS–NIR spectrum analysis

UV–visible–near infrared electronic absorption and transmission spectrum shown in Fig. 7a, b was obtained by scanning the sample over the wavelength range of 200–800 nm using Varian Carry 5000 spectrophotometer. This data helps us to get an idea about the activation energy required for the electronic excitation as well as the strength of the basic bonding present within the material. Large charge transfer

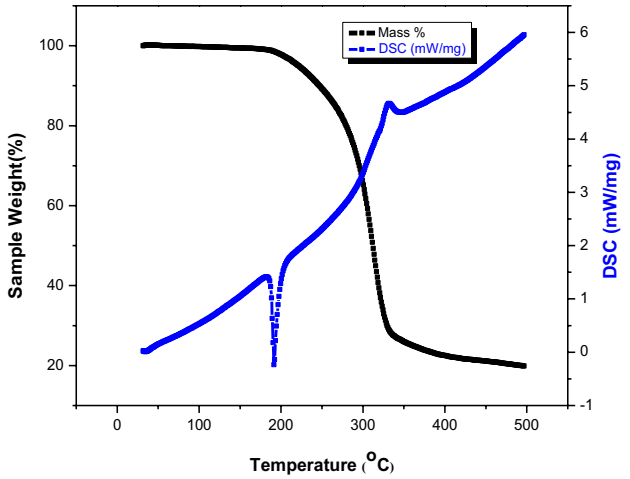

Fig. 6 Thermal degradation pattern of the DMAPDNBA complex

with fever dislocation density within the material is considered as the essential criterion to achieve promising optical transparency in organic NLO crystals. The lower cutoff wavelength and a large transparency in the UV–VIS region seems to be a vital requirement for NLO crystals to be used in optoelectronic applications, laser threshold applications and higher harmonic generations for practical applicability [29, 30].The moderate absorption band that appears as a hump at 227 nm near the UV region is mainly attributed to the n–π^* transition due to the presence of the NH_2 group within the material and it also holds some basic information regarding π–π^* electronic transitions occurring in the aromatic ring of the phenyl group. Here, the absence of absorption between 400 and 800 nm in the visible and near IR region strongly enables the system to be a probable aid in generating hyperpolarizable potential for the frequency conversion [31]. The percentage of transmittance is about 95% throughout the visible window, which recommends the good optically transparent complex as an excellent candidate suitable for laser-assisted non-linear optical applications.

3.4.1 Determination of absorption edge and optical band gap energy

The fundamental absorption observed in the UV–VIS–NIR spectra corresponding to the electron excitation between the valence band and conduction band helps us to determine the nature and value of the optical band gap using the relation:

$$E_g = \frac{1240}{\lambda}\ \text{eV}. \tag{5}$$

For a lower cutoff wavelength of 227 nm, it was found to be 5.46 eV. The direct optical band gap energy of the grown DMAPDNBA complex can also be calculated exploiting the dependence of photon energy($h\upsilon$) upon absorption coefficient(α) supported by the equation:

$$(\alpha h\upsilon)^2 = A^*\left(h\upsilon - E_g\right), \tag{6}$$

where $\alpha = 2.3036^*A/t$ with 'A' as the absorbance of the material. By extrapolating the straight line graph plotted between $(\alpha h\upsilon)^2$ and E_g (eV) as in Fig. 8, the direct optical band gap energy was found to be 5.45 eV which agrees well with that of the value obtained via the absorption spectrum.

The linear optical parameters such as refractive index (n), optical reflectance (R) and electric susceptibility(χ_c) of the

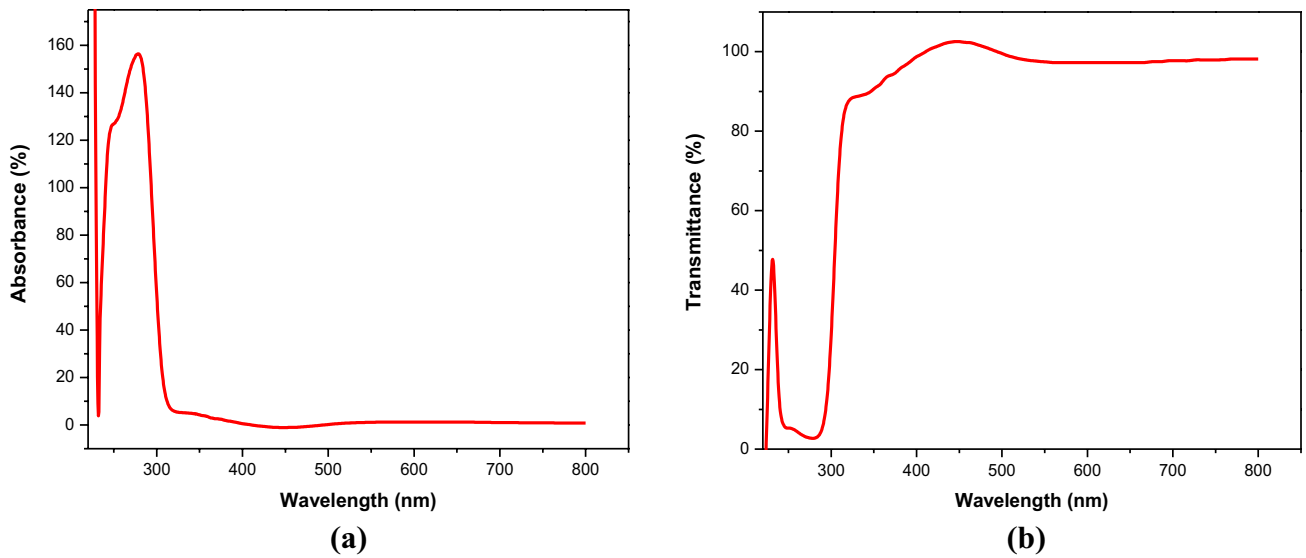

Fig. 7 **a** Absorption spectrum and **b** transmission spectrum of the DMAPDNBA complex

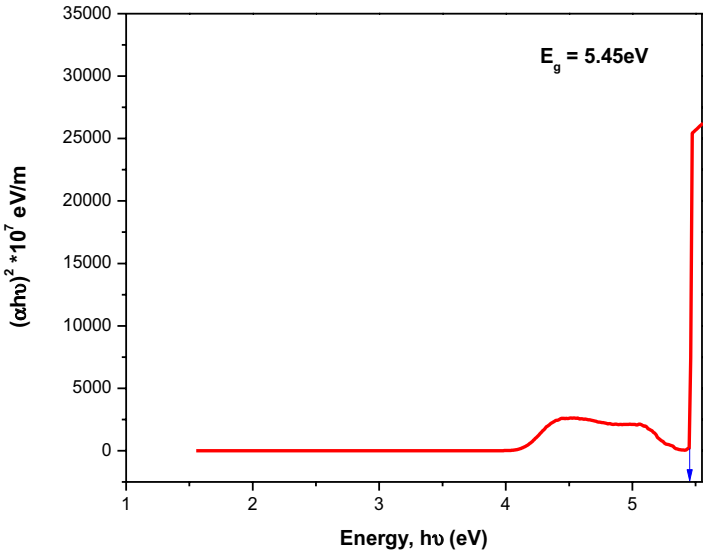

Fig. 8 Tauc's plot for determining optical band gap of the complex, DMAPDNBA

Table 4 Optical parameters of the DMAPDNBA crystal

Optical parameters	Values
Cutoff wavelength (λ)	227 nm
Band gap energy (E_g)	5.45 eV
Transmittance	90%
Refractive index (n)	2.35
Optical reflectance (R)	0.16
Electric susceptibility (χ_c)	4.50

material can be estimated by performing the following formulations and the obtained values are shown in Table 4:

$$n^4(E_g - 0.365) = 154, \tag{7}$$

$$R = \frac{(n-1)^2}{(n+1)^2}, \tag{8}$$

$$\chi_c = n^2 - 1. \tag{9}$$

3.5 Fluorescence studies

Photoluminescence study reveals the direct information about the crystalline quality, structural perfection and physical

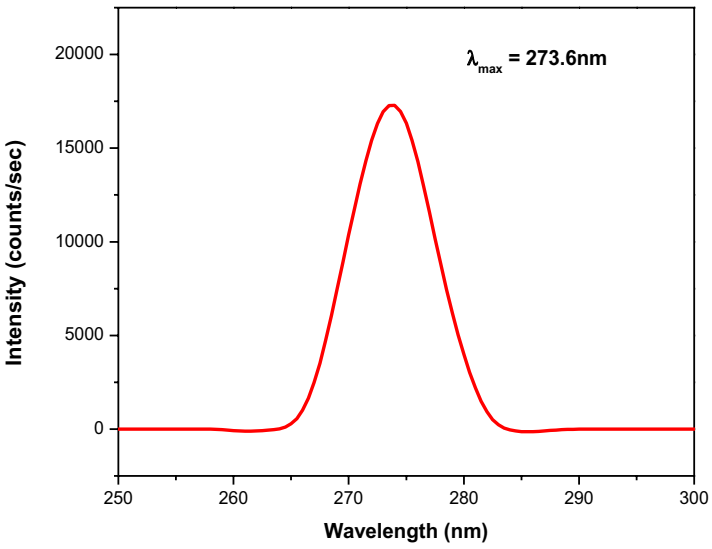

Fig. 9 Fluorescence spectrum of the DMAPDNBA complex

properties of materials apart from the fluorescent property, since the intensity of the curve strongly depends on those parameters [32]. The luminescence property will be sufficiently exhibited by materials having defect-free lattice sites and aromatic rings with prolonged conjugated double bonds [33]. Here, the luminescence spectrum (Fig. 9) was obtained with the excitation wavelength of 227 nm, cross matched with the UV–VIS–NIR spectrum and the Tauc's plot, and the corresponding emission spectrum was recorded in the wavelength range of 250–300 nm which results in a sharp intensified emission peak near the UV region at 273.6 nm. The absence of visible emission bands in the luminescent spectrum agrees well with the UV spectrum showing no significant absorption near the second harmonic generation (SHG) signal, one of the prominent properties which must be satisfied by all non-linear optical materials [34].

3.6 Microhardness analysis

The hardness of the grown DMAPDNBA was examined by using Vickers microhardness tester employed with a pyramidal indenter. It seems to be a prominent technique to estimate the mechanical stability of the material which in turn provides an idea of elastic constants and yield strength [35, 36]. The well-polished crystal was placed over the microhardness tester and was subjected to various loads ranging from 20 to 100 g and an indentation mark was made on the surface of the material using a diamond-shaped indenter. To obtain the hardness of the material, the average diagonal length of the indenter pierced into the crystal surface of the sample was measured using Leitz Metallax II Microscope. As the load increases, the hardness number also increases up to 60 g obeying reverse indentation size effect (RISE) and beyond 60 g internal stress was generated within the material due to indentation [37]. Above 60 g, crystals start undergoing deformation leaving dislocations in the form of cracks near the indentation sites. The maximum extent up to which a material can hold elasticity or can withhold microcracks can be defined as the hardness of a particular material to deformation. The entity used to explain that property is termed as the hardness number of a material. Figure 10 explains how this property is related to the applied load and is expressed as;

$$H_{\mathrm{v}} = \frac{1.8544P}{d^2}. \tag{10}$$

Here, P and d refers to the applied load (g) and diagonal length (mm), respectively.

Onitsch [38] and Hanneman [39] proposed a co-relation connecting the applied load (P) and the diagonal length of impression(d) as

$$P = ad^n. \tag{11}$$

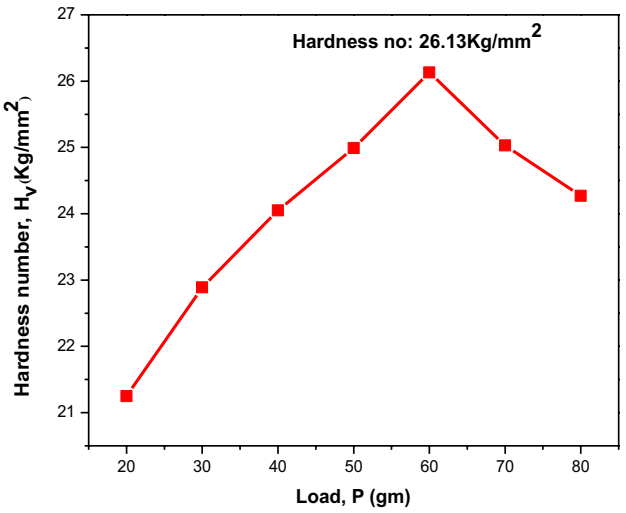

Fig. 10 Variation of hardness of the complex DMAPDNBA with that of the applied load

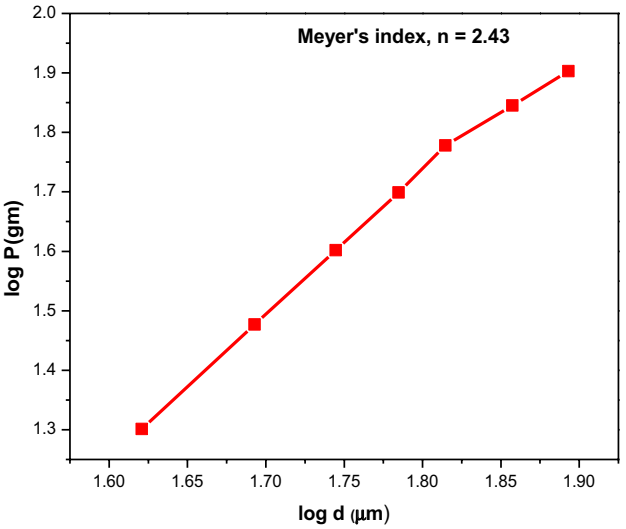

Fig. 11 Meyer's plot of the grown DMAPDNBA crystal

Here, 'a' is the constant of proportionality and 'n' is termed as the Meyer's index number. It can be rearranged using the logarithmic function as

$$\log\ P = \log\ a + n\log d. \tag{12}$$

Meyer's number was then calculated from the plot of log P versus log d and the slope of the curve by least square fitting gives the value of 'n' as 2.43 for the DMAPDNBA material. Since the obtained value of 'n' for the grown complex is greater than 1.6, it confirms that the obtained compound belongs to the category of soft material [39–42] (Fig. 11).

Table 5 Mechanical parameters of the DMAPDNBA crystal

Mechanical parameters	Values
Hardness number (H_v)	26.13 kg/mm^2
Meyer's index(n)	2.43
Stiffness constant	(C_{11}) 3.01*10^2 N/m
Yield strength (σ_y)	13.48 kg/mm^2

The mechanical stability of the DMAPDNBA crystal can be ensured through certain parameters such as stiffness constant and yield strength (Table 5). The values corresponding to the hardness number and the behaviour of those parameters with the applied load are illustrated through Fig. 12a, b.

$$C_{11} = (H_v)^{(7/4)}, \tag{13}$$

$$\sigma_y = \frac{(3-n)}{2.9}\left[\frac{12.5(n-2)}{(3-n)}\right]^{(n-2)} H_v, n > 2, \tag{14}$$

$$\sigma_y = \frac{H_v}{3}, n < 2. \tag{15}$$

3.7 Dielectric studies

The dielectric behaviour of the material gives information regarding the lattice dynamics of the crystal by analysing the distribution of the electric field within the material [43]. The cut and polished crystals of the as-grown charge transfer complex electroded with silver paste were subjected to dielectric studies using HIOKI 3532 LCR HITESTER. Mostly, the organic compounds exhibit promising dielectric response at low frequencies. From the observed value of parallel capacitance, the dielectric constant was calculated using the expression:

$$\text{Dielectric constant}, \varepsilon_r = \frac{C_p d}{\varepsilon_0 A}. \tag{16}$$

The variation of the calculated dielectric constant of the sample with log of frequency for various temperatures is plotted in Fig. 13. From the graph, it can be noticed that there is a rise in the dielectric constant value at the low-frequency region/high temperature attributed to four types of polarization mechanisms, namely electronic, space charge, dipolar and ionic polarizations, within which the distortion of space charge plays a vital role [44, 45], and low dielectric constant values in higher-frequency regime/lower temperature tend to redistribute the lattice defects and thereby result in a screening effect [13]. But only a marginal change was observed due to the negligible thermal activation and stable positions of the lattice charges. In other words, it can be very well understood that the value of dielectric constant decreases exponentially and thus attains a constant value at higher frequencies independent of the temperature. This constant value at higher frequency reveals the superior optical quality of the material which can be effectively employed for various NLO applications [46–48]. In general, the dielectric constant follows a periodic trend in their nature with temperature at varied frequencies. From the plots, it can be

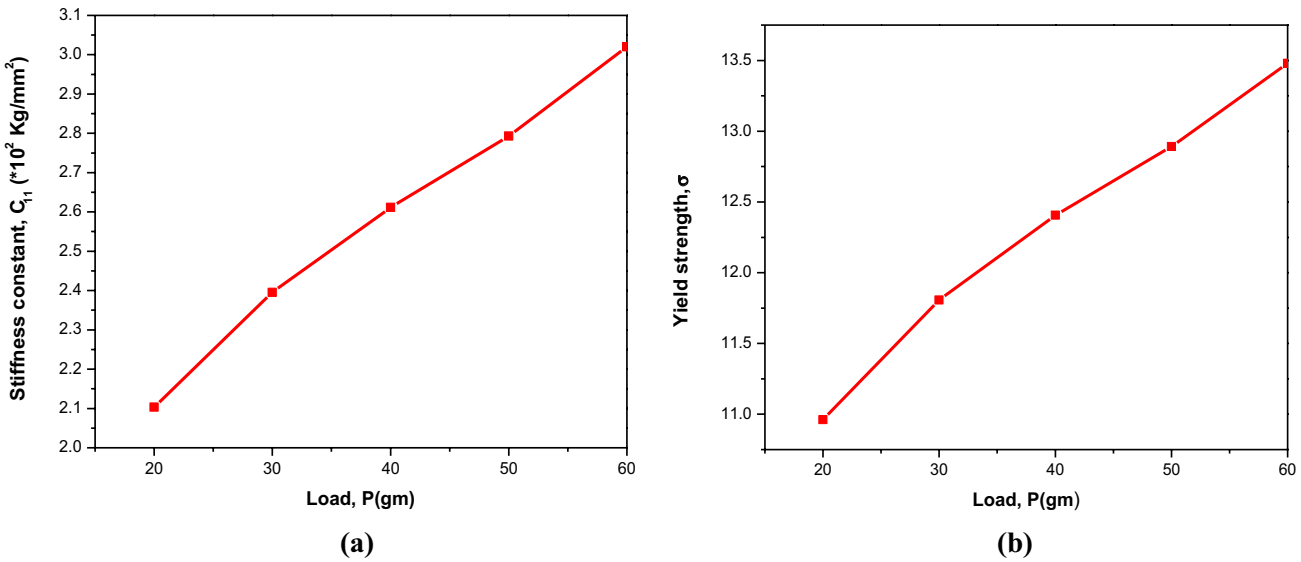

Fig. 12 **a** Variation of stiffness constant (C_{11}) and **b** variation of yield strength (σ_y) with the applied load (P)

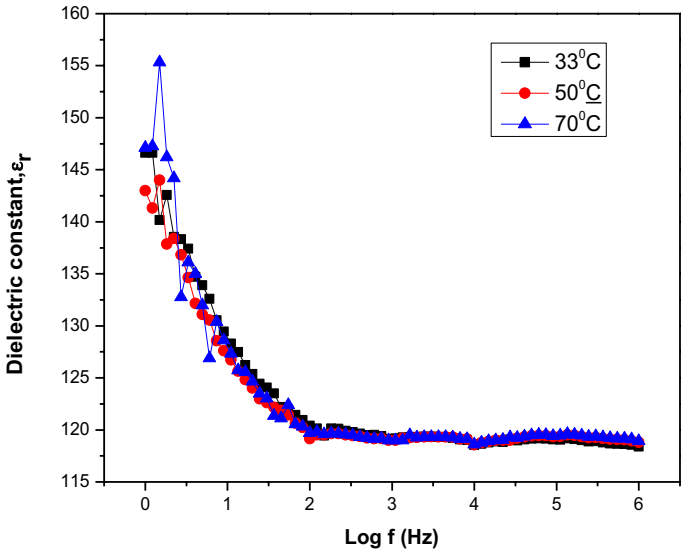

Fig. 13 Variation of dielectric constant with the log of the applied frequency

inferred that the conduction mechanism occurs by proton hopping via hydrogen bonds or by ions over the barrier between two sites.

3.7.1 Determination of solid-state parameters

The electronic polarizability can be evaluated exploiting two approaches, namely Penn gap analysis and Clausius–Mossotti analysis. For executing the calculation process, primarily some quantities such as valence electron plasma energy, Penn gap energy and Fermi energy have to be determined. The valence electron plasma energy is related by

$$\hbar\omega_p = 28.8\sqrt{\frac{Z\rho}{M}}, \tag{17}$$

where Z is the total number of valence electrons in the DMAPDNBA crystal, ρ is the density of the sample, M is the molecular mass of the crystal and ω_p is defined as the plasma angular frequency. For the DMAPDNBA crystal, Z value was estimated to be 126, $\rho = 1.471$ g/cm^3 and $M = 334.29$ g/mol.

Thus, the Penn gap E_p and Fermi energy E_f can be defined as:

$$E_p = \frac{\hbar\omega_p}{\sqrt{(\varepsilon_r - 1)}}, \tag{18}$$

$$E_f = 0.2948(\hbar\omega_p)^{4/3}. \tag{19}$$

The polarizability (α) can be accounted from the Penn gap approach as:

$$\alpha = \left[\frac{(\hbar\omega_p)^2 S_0}{(\hbar\omega_p)^2 S_0 + 3E_p^2}\right]\frac{M}{\rho} \times 0.396 \times 10^{-24}\ \text{cm}^3, \tag{20}$$

where S_o is a constant for any material,

$$S_0 = 1 - \left[\frac{E_p}{4E_f}\right] + \frac{1}{3}\left[\frac{E_p}{4E_f}\right]^2.$$

The electronic polarizability α can be found using the Clausius–Mossotti approach as:

$$\alpha = \frac{3M}{4\pi N_a \rho}\left(\frac{\varepsilon_r - 1}{\varepsilon_r + 2}\right), \tag{21}$$

where N_a is the Avogadro number. The obtained electronic polarizability properties are exhibited in Table 6 and are

Table 6 Electronic polarizability parameters of the DMAPDNBA complex

Polarizability parameters	Present study	KDP values
Electron plasma energy($\hbar\omega_p$)	21.44 eV	17.33 eV
Penn gap energy (E_p)	1.98 eV	2.39 eV
Fermi energy (E_f)	17.56 eV	12.02 eV
Polarizability (α) (Penn gap analysis)	8.77*10^{-23} cm^3	2.14*10^{-23} cm^3
Polarizability (α) (Clausius–Mossotti equation)	8.79*10^{-23} cm^3	2.18*10^{-23} cm^3

compared with the standard NLO material, potassium dihydrogen phosphate (KDP), for establishing the candidature of DMAPDNBA crystal in laser-assisted optical technologies.

3.8 Laser damage threshold study

NLO crystals with high optical surface damage threshold for longer duration are largely demanded by non-linear optical operations such as electro-optic modulation, second harmonic generation and terahertz wave generation [49]. Hence, the ability of the material to withstand the energy of the incoming laser radiation has to be strictly verified. The property of surface damage mainly depends on laser parameters such as the spatial profile of the pulse (duration, width, energy) and on the interstitial factors such as defects and dislocations within the crystal lattice [50, 51]. Hence, the threshold value is defined to be the lowest laser intensity that can be tolerated by the crystal surface without getting damaged. The damage mechanism originates from the simultaneously occurring effects such as multi-photon absorption, avalanche ionization and photo-ionization of the crystal due to thermal agitation [49]. LDT measurement was performed under Q-switched mode-operated Nd:YAG laser beam (single shot mode, 1064 nm, 9 ns, 10 Hz). The DMAPDNBA crystal was subjected to laser beam energy ranges from 5 mJ to 53 mJ and a small spot-like crack was observed on the sample surface by the input laser intensity of 53 mJ. The corresponding power density can be calculated using the expression:

$$P_{\mathrm{d}} = \frac{E}{\tau A}, \tag{22}$$

where E is the laser beam energy (mJ), τ the pulse width (ns) and A is the area of the circular spot (πr^2) impinging on the DMAPDNBA crystal during the measurement. The LDT value of the sample is compared with that of KDP and urea as shown in Table 7.

The estimated LDT value for the crystal is 1.74GW/cm^2, which is far better when compared with the cutoff value for the KDP and urea crystals. Hence, the present study reveals the efficiency of the grown NLO crystal of DMAPDNBA for its usage in photonic devices where laser damage threshold value has a challenging character.

Table 7 Comparison of LDT values with standard materials

Compound	LDT (GW/cm^2)
PNBPDA	1.74
KDP	0.20
Urea	1.50

3.9 Second harmonic generation studies

In the present study, the efficiency of the SHG was evaluated using Kurtz and Perry powder technique and this measurement helps us to find materials suitable for executing non-linear optical operations. Here, a fine powdered sample of the grown crystal was filled in a capillary tube and placed in the path of a Q-switched Nd:YAG laser of wavelength 1064 nm, which serves as monochromatic laser beam with input energy of 0.69 J holding frequency and pulse repetition rate of 10 Hz and 10 ns, respectively [52]. The presence of SHG signal (2ω) was thus confirmed through the emission of a green light of wavelength 532 nm and hence the value of effective susceptibility of the DMAPDNBA complex was determined to be same as that of the inorganic reference material, potassium dihydrogen phosphate (KDP), under consideration. It was calculated by evaluating the output voltage obtained through the analysis, i.e. 30 mV for KDP and 0.24 V for the DMAPDNBA material, as well as the output of organic urea was found to be 75 mV with which we can infer the frequency conversion of DMAPDNBA with that of urea as 3.2 times. The presence of non-linearity within the material might be due to the asymmetric distribution of π-electron cloud density. This structural modification resulting from the intermolecular charge transfer between the methyl groups and phenyl groups inhibits the strength of dipole interactions and thereby enhances the non-linear behaviour of DMAPDNBA material [53] (Table 8).

3.10 Z-scan measurement

Third-order non-linear measurements were conducted by the most sensitive Z-scan technique proposed by Bahae

Table 8 Comparison of the SHG value of the DMAPDNBA crystal with some reported pyridine derivatives

Some Pyridine derivatives	SHG values (as multiple of KDP)
4-Dimethylaminopyridine copper chloride	0.47 [14]
4-Dimethylaminopyridine potassium chloride 2-aminopyridine	0.60 [15]
4-Dimethylaminopyridine potassium chloride	0.69 [16]
4-Dimethylaminopyridinium-3,5-dicarboxybenzoate	0.89 [17]
4-Dimethylaminopyridinium 3,5-dinitrobenzoate	8 [Present work]

et al. [54]. Materials possessing significant third-order optical non-linearity with ultrafast response time are challenged by the optoelectronic applications such as during the fabrication of lasers, optical switching, computing and limiting [51]. To perform the Z-scan experiment, the sample solution of 0.01 M concentration filled in a cuvette was translated through the focus along the z-direction using a computer-controlled setup. The corresponding transmitted pulse energy with (closed aperture) or without (open aperture) a far-field aperture was recorded by the photo detector and the intensity was measured digitally. Thus, the Z-scan trace can be defined as the profile of the transmitted intensity that passes through the sample as a function of the sample position [51]. In the open aperture method, the entire transmitted laser beam was caught by the detector to evaluate its non-linear absorption coefficient, while an aperture will be placed between the lens and the detector in the closed aperture arrangement to determine the non-linear refraction of the grown DMAPDNBA crystal.

The non-linear absorption coefficient of the crystal is evaluated by fitting the experimentally obtained open aperture curve with the transmission equation obeying a two photon absorption process:

$$T(z, s=1) = \sum_{m=0}^{\infty} \left[\frac{\{-q_0(z,0)\}^m}{[m+1]^{3/2}} \right], |q_0| < 1, \tag{23}$$

where $q_0(z,0) = \beta I_0(t) L_{\text{eff}}$ and $L_{\text{eff}} = \frac{(1-e^{-\alpha l_0})}{\alpha}$ is the effective thickness of the sample with the linear absorption coefficient α and I_0 is the incoming intensity of the laser beam at the focus. Hence, the non-linear absorption coefficient can be determined by:

$$\beta = \frac{q_0(z,0)}{I_0(t) L_{\text{eff}}}. \tag{24}$$

The imaginary part of the third-order susceptibility $\text{Im}\chi^{(3)}$ was formulated from β through the relation:

$$\text{Im}\chi^{(3)}(\text{esu}) = \frac{(10^{-2}\varepsilon_0 n_0^2 c^2 \lambda \beta)}{4\pi^2}\ (\text{cm/W}), \tag{25}$$

where ε_0 is the permittivity of free space, n_0 is the linear refractive index and c is the velocity of light in vacuum. The non-linear refractive index of DMAPDNBA compound was investigated by performing closed aperture Z-scan technique. The normalized transmittance $T(z)$ is given by:

$$T(z, \Delta\varphi_0) = 1 - \frac{4\Delta\varphi_0 x}{(x^2+9)(x^2+1)}, \tag{26}$$

where $\Delta\phi_0$ is represented as the on-axis non-linear phase shift and x is defined as z/z_0. The non-linear refractive index n_2 of the DMAPDNBA complex can be estimated as

$$n_2 = \frac{\Delta\varphi_0 \lambda}{2\pi I_0 L_{\text{eff}}}, \tag{27}$$

where $\Delta\varphi = \frac{\Delta T_{p-v}}{0.406(1-S)^{0.25}}$.The evaluated $\Delta T_{\text{p-v}}$ is expressed as the difference between the peak (T_{p}) and valley transmittance (T_{v}) values. The linear transmittance in a closed aperture approach 'S' is connected by the relation:

$$S = 1 - \exp\left(-2r_{\text{a}}^2/\omega_{\text{a}}^2\right).$$

The real part of non-linear susceptibility, $\text{Re}\,\chi^{(3)}$, is provided by the relation:

$$\text{Re}\chi^{(3)}(\text{esu}) = \frac{\left(10^{-4}\varepsilon_0 n_0^2 c^2 n_2\right)}{\pi}(\text{cm}^2/\text{W}). \tag{28}$$

The third-order non-linear susceptibility, $\chi^{(3)}$ was calculated from the relation:

$$\chi^{(3)} = \left[(\text{Re}\chi^{(3)})^2 + (\text{Im}\chi^{(3)})^2\right]^{1/2}. \tag{29}$$

Various properties of the materials like focusing nature and refractive index character can be identified from the open and closed aperture plots of the Z-scan experiment. Here, the open aperture Z-scan transmittance curve (Fig. 14a) of the DMAPDNBA sample exhibits minimum transmittance when translated towards the focus ($z=0$) and the intensity goes on increasing when moved away from the focus. This represents the reverse saturable absorption (RSA) phenomenon, probing positive value for the non-linear absorption coefficient. The RSA effect has been noticed in π-conjugated organic materials [55] and the occurrence of this behaviour is mainly attributed to the multi-photon absorption (MPA) process and excited state absorption (ESA) effect, reflecting the population dominance in the area of cross section of higher state when compared to the ground state [56, 57]. On the other hand, the closed aperture curve (Fig. 14b) facilitates the grown crystal to have non-linear refraction of positive nature, illustrated by a valley followed by a peak, and demonstrates the self- focusing ($n_2 > 0$) signature of the DMAPDNBA material.

The second-order hyperpolarizability, Υ, of the sample is related to the third-order susceptibility through the equation:

$$\gamma = \frac{\chi^{(3)}}{\left[\frac{1}{3}(n_0^2+2)\right]^4 N}, \tag{30}$$

where N is the molecular number density in cm^3. This enhanced values of $\chi^{(3)}$ and Υ of the DMAPDNBA compound recommend its resourceful efficiency that can be consumed by non-linear optical devices. A new factor that facilitates the non-linear response is termed as the coupling

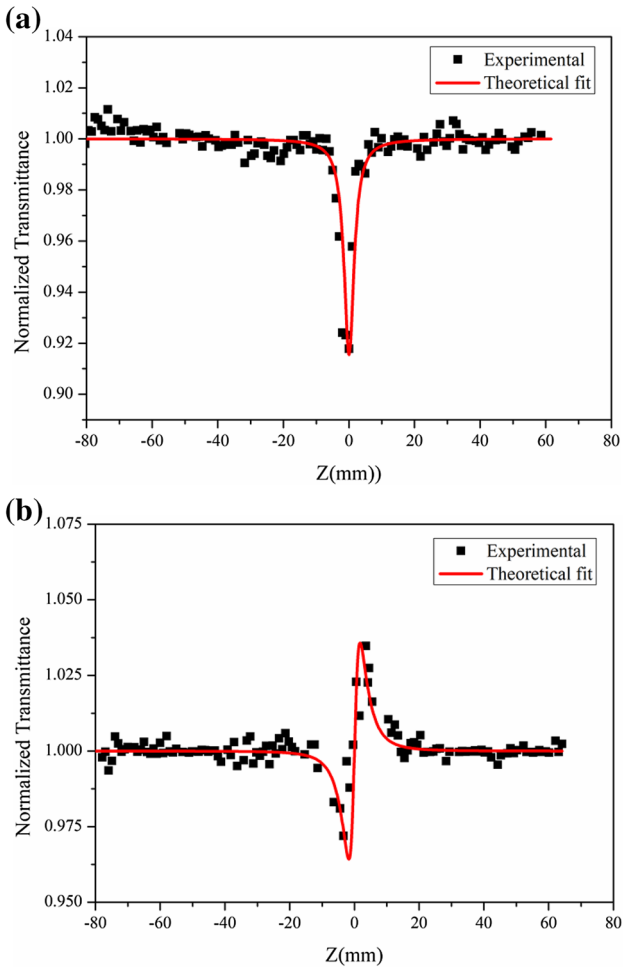

Fig. 14 **a** Open aperture curve, **b** closed aperture curve

factor (ρ) and is expressed in terms of the imaginary part of $\chi^{(3)}$ and the real part of $\chi^{(3)}$, as follows:

$$\rho = \frac{\mathrm{Im}\chi^{(3)}}{\mathrm{Re}\chi^{(3)}}. \tag{31}$$

Optical resolution of Z-scan setup
Laser excitation wavelength (λ) = 532 nm
Focal length of the lens used (f) = 10 cm
Beam waist radius (ω_a) = 1.5 mm
Aperture radius (r_a) = 1 mm
Effective thickness of the sample (L_{eff}) = 0.995*10^{-3} m
Incident intensity at the focus (I_0) = 7.011*10^{13} W/m^2
On-axis phase shift at the focus ($\Delta\varphi_0$) = 0.727
Linear refractive index (n_0) = 3.635

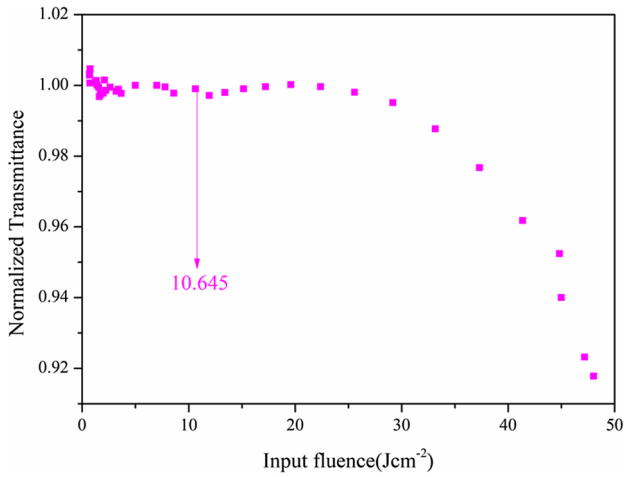

Fig. 15 Optical limiting curve of the DMAPDNBA crystal

3.10.1 Optical limiting property

Optical limiting property can be observed in materials, when the transmitted intensity decreases with an increase in the input fluence/laser intensity. This property can be achieved by exploiting various optically active non-linear mechanisms such as multi-photon absorption (MPA), self-focussing/defocussing, excited state absorption (ESA), non-linear scattering and free carrier absorption (FCA) [58]. To characterize the optical limiting behaviour of the sample, the transmission of the medium is recorded with the input intensity in the range of about 0–50 J/cm^2. The non-linear transmittance was observed to be decreasing at 10.645 J/cm^2 and this particular value of input fluence is termed as the threshold intensity of the optical limiting. Optical limiting threshold value can be defined as the minimum input intensity demanded by the laser beam to execute the deviation from non-linearity (to decrease the transmission intensity) and thereby reducing the highly intensified output power causing irritation to the naked eyes and sensitive instruments. The lower the threshold value, the better will be the optical limiting behaviour of the material. The optical limiting plot as depicted in Fig. 15 is extracted from the open aperture z-scan data through the relation:

$$I_z = \frac{I_0}{1 + \left(\frac{z^2}{z_0^2}\right)},$$

where $I_0 = \frac{E}{\pi\omega_0^2\tau}$ and E represent the laser beam energy in joules.

The low O_{LT} value of the DMAPDNBA sample of 10.645 J/cm^2 illustrates the significant optical limiting nature of the material which plays a key role in most of the recently discovered optoelectronic devices.

The optical switching performance of the material can be predicted by estimating the figure of merit (FOM) parameter supported by two photon absorption theory given as:

$$F = \frac{2\beta\lambda}{n_2}, \tag{32}$$

where λ is the Z-scan operating wavelength (532 nm).

The magnitude of $F > 1$ seems to be the essential criteria for the material to be used in optical integrated devices. The evaluated value of FOM is 5.84, which is very much larger than the numerical value 1. Hence, the developed crystals of DMAPDNBA offer fascinating applications in the opto-electronics domain (Table 9).

3.11 Quantum computational analysis

3.11.1 Molecular geometry

The optimized geometry of the title compound was obtained from the crystallographic information file (CIF) available with the reported literature. The derived geometry was then visualized with Chemcraft [59] software and further investigations were carried out under density functional level of theory (DFT) with B3LYP/6-31G*d(p) basis set functionalism using Gaussian 09 software.

3.11.2 Frontier molecular orbital (FMO)/HOMO–LUMO analysis

Frontier molecular orbital analysis helps us to explore various properties of molecules including chemical stability/chemical reactivity and charge transfer interaction between the molecules which paves the way for a better understanding of the NLO response of a material [60].

Table 9 Non-linear optical parameters of the DMAPDNBA compound from Z-scan study

Non-linear optical properties	Values
SHG efficiency	8 times that of KDP
LDT at 1064 nm	1.74 GW/cm^2
Non-linear absorption coefficient (β)	4.83*10^{-12} m/W
Non-linear refractive index (n_2)	8.79*10^{-19} m^2/W
Imaginary part of susceptibility (Im($\chi^{(3)}$))	6.86*10^{-13} esu
Real part of susceptibility (Re($\chi^{(3)}$))	29.50*10^{-13} esu
Third order non-linear susceptibility ($\chi^{(3)}$)	30.28*10^{-13} esu
Second-order hyperpolarizability (Υ)	7.60*10^{-34} esu
Coupling factor (ρ)	0.23
Optical limiting threshold (O_{LT})	10.645 J/cm^2
Figure of merit (FOM)	5.84

The FMO calculation is carried out based on the excitation of an electron from the highest occupied molecular orbital (HOMO) to the lowest unoccupied molecular orbital (LUMO). In the DMAPDNBA sample, the pyridine moiety of dimethylamino group act as the electron donating group whereas the benzoic acid moiety in dinitrobenzoic acid molecule act as the electron withdrawing group. The HOMO–LUMO separation will be then evaluated for predicting the efficiency of proton transfer interaction and thereby concluding the occurrence of molecular polarizability which primarily serves as the cause of non-linear behaviour within the molecules [61]. The energy gap was found to be 3.484 eV. The smaller HOMO–LUMO energy gap characterizes less stability and more reactivity property of the molecule which enhances the molecular polarizability through an efficient charge transfer interaction.

3.11.3 Molecular electrostatic surface potential (MESP) analysis

MESP serves as a key feature in computational analysis to examine the electronic and protonic charge distribution produced by the total electron density within the molecule [62]. This three-dimensional plot of electrostatic effect reflects the polarity, dipole moment and the chemically reactive sites extended over the molecule [61]. The organic molecules under delocalized pi electron perspective are found to be significantly influenced by the external optical fields, since the delocalized orbitals are extended over the entire molecular structure giving rise to large polarization [62]. The most positive electrostatic potential region is represented by blue colour, which indicates the electron-deficient site encouraging nucleophilic attack. On the other hand, red colour represents the electron-rich zone, which serves as the most negative potential region related to the electrophilic nature of the molecule, and the charge-depleted or the zero potential sites are pictured by green code which acts as the medium for the charge transfer interaction. Here, the most negative potential is extended over the dimethylamino groups of the pyridine moiety and the most positive potential region is illustrated by the oxygen atoms in the benzoic acid group. There is possibility of proton transfer mechanism taking place between the dimethylamino component of the electrophilic group and the oxygen atoms located in the nucleophilic site of the 3,5-dinitrobenzoic molecule. The resultant interaction strongly agrees with the NLO activity exhibited by the molecule as confirmed through the HOMO–LUMO studies (Fig. 16).

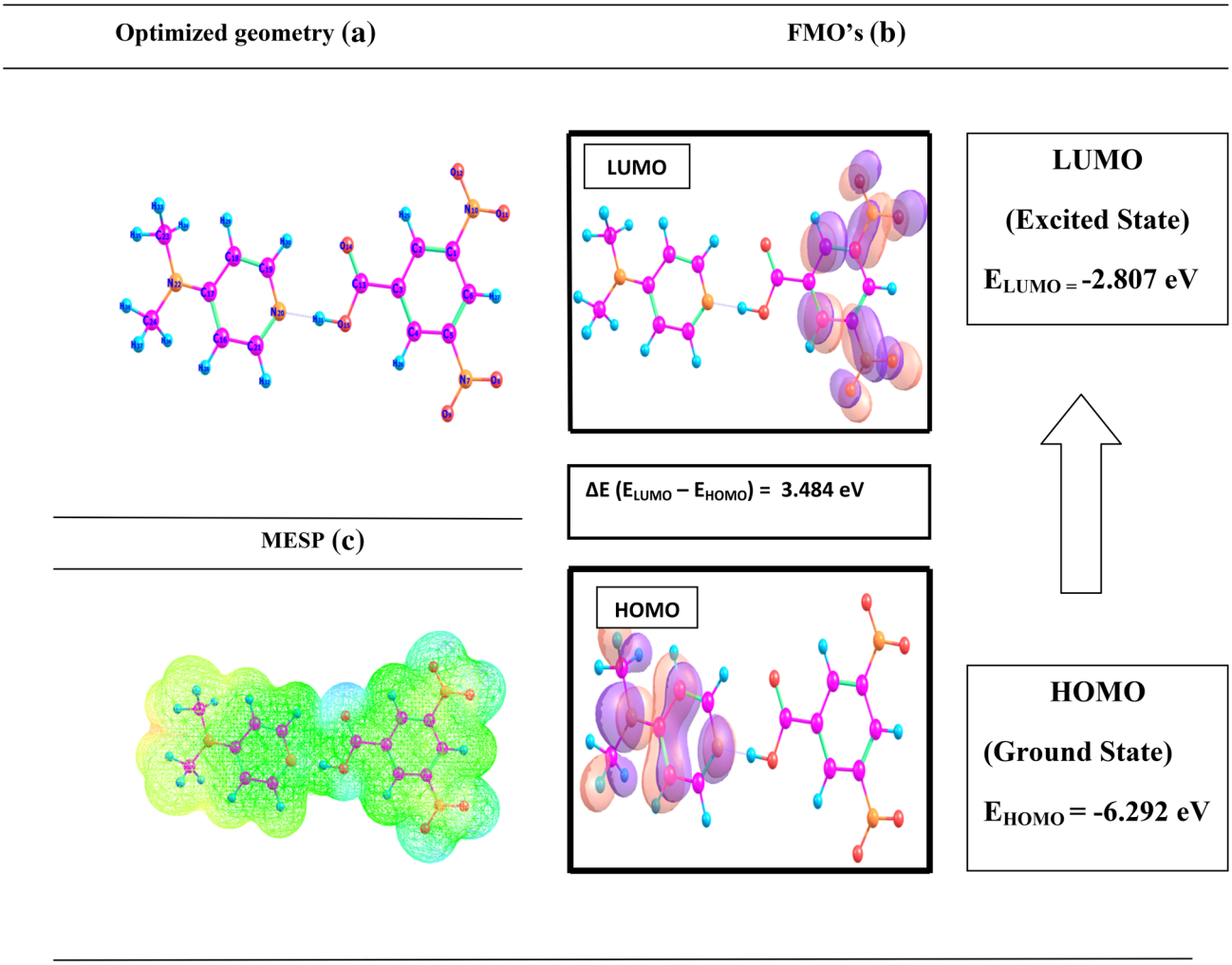

Fig. 16 **a** Optimized geometry, **b** FMO analysis, **c** pictorial representation of MESP

3.11.4 Non-linear optical property calculations

The quantum computational calculations were conducted to measure the theoretical values of NLO parameters of the DMAPDNBA molecule. Various non-linear electronic properties such as electric dipole moment, electric polarizability and hyperpolarizability were exploited to understand the structure–property relationship of a molecule attributed to its NLO characteristics. This non-linear optical response of the system is directly linked with the intramolecular charge transfer interaction originated from the drifting of an electron cloud from an electron-donating group to the electron-withdrawing group through an efficient pi-conjugated bridge framework [62]. All the above-mentioned electronic properties were then evaluated theoretically under gaseous phase background to verify the strength of the non-linear optical activity of the molecule. Here, the organic molecule, urea, is selected to be the prototypical molecule in comparing the non-linear properties of the molecular system, since it plays a vital role in non-linear studies.

$$\text{Dipole moment, } \mu = (\mu_x^2 + \mu_y^2 + \mu_z^2)^{1/2}, \tag{33}$$

$$\text{Polarizability, } \alpha = \frac{(\alpha_{xx} + \alpha_{yy} + \alpha_{zz})}{3}, \tag{34}$$

$$\text{First - order hyperpolarizability, } \beta = (\beta_x^2 + \beta_y^2 + \beta_z^2)^{1/2}, \tag{35}$$

where $\beta_x = \beta_{xxx} + \beta_{xyy} + \beta_{xzz}$, $\beta_y = \beta_{yyy} + \beta_{yxx} + \beta_{yzz}$ and $\beta_z = \beta_{zzz} + \beta_{zxx} + \beta_{zyy}$.
Second-order hyperpolarizability:

$$\gamma = \frac{1}{5}(\gamma_{xxxx} + \gamma_{yyyy} + \gamma_{zzzz} + 2\gamma_{xxyy} + 2\gamma_{xxzz} + 2\gamma_{yyzz}). \tag{36}$$

Table 10 Non-linear optical components of DMAPDNBA molecule

Dipole moment (μ) components (Debye, D)		
	B3LYP/	HF/
μ_x	12.326	− 12.034
μ_y	− 0.431	0.570
μ_z	0.004	0.004
μ_{total} (Debye) 12.325D 12.047D		
Linear polarizability (α) components (atomic unit, a.u)		
	B3LYP/	HF/
α_{xx}	− 102.294	− 112.864
α_{yy}	− 152.756	− 158.660
α_{zz}	− 135.470	− 138.916
α_{xy}	1.563	1.064
α_{xz}	0.046	− 0.060
α_{yz}	0.004	− 0.004
α_{total} (a.u)	− 130.173 a.u	− 136.8133 a.u
α_{total} (esu)	$-1.953*10^{-23}$ esu	$-2.052*10^{-23}$esu
First-order hyperpolarizability (β) components (atomic unit, a.u)		
	B3LYP/	HF/
β_{xxx}	701.381	− 708.597
β_{yyy}	0.661	1.032
β_{zzz}	0.021	0.022
β_{xyy}	132.193	− 158.525
β_{xxy}	10.456	− 6.077
β_{xxz}	0.176	0.187
β_{xzz}	− 38.597	40.262
β_{yzz}	0.963	− 1.002
β_{yyz}	− 0.019	− 0.024
β_{xyz}	0.001	0.001
β_x	620.314	687.791
β_y	48.421	− 47.535
β_z	− 9.703	12.63
β_{total} (a.u)	795.069 a.u	826.882 a.u
β_{total} (esu)	$6.869*10^{-30}$esu	$7.144*10^{-30}$esu
Second-order hyperpolarizability (γ) components (atomic unit, a.u)		
	B3LYP/	HF/
γ_{xxxx}	− 15,218.779	− 15,953.062
γ_{yyyy}	− 2700.957	− 2796.225
γ_{zzzz}	− 136.173	− 142.986
γ_{xxxy}	199.559	200.841
γ_{xxxz}	2.517	− 2.767
γ_{yyyx}	− 7.438	− 14.256
γ_{yyyz}	0.026	− 0.031
γ_{zzzx}	− 0.034	0.025
γ_{zzzy}	− 0.011	0.012
γ_{xxyy}	− 3719.349	− 3883.730
γ_{xxzz}	− 3004.051	− 3084.445
γ_{yyzz}	− 409.601	− 420.306
γ_{xxyz}	0.043	− 0.044
γ_{yyxz}	0.101	− 0.131
γ_{zzxy}	2.624	2.822
γ_{total} (a.u)	− 6464.382	− 6733.847
γ_{total} (esu)	$-3.258*10^{-36}$esu	$-3.394*10^{-36}$esu

Table 11 Non-linear optical parameters obtained from computational analysis

Non-linear optical parameters	From B3LYP	From HF
Dipole moment (μ)	12.32 debye	12.05 debye
Polarizability (α)	$-1.95*10^{-23}$ esu	$-2.05*10^{-23}$ esu
First-order polarizability (β)	$6.87*10^{-30}$esu	$7.14*10^{-30}$ esu
Second-order hyperpolarizability (γ)	$-3.26*10^{-36}$esu	$-3.39*10^{-36}$ esu

The dipole moment (μ) of the DMAPDNBA molecule ($\mu = 12.325$D) was found to be 5.2 times that of the standard reference material of organic urea ($\mu = 2.3732$D) and the first-order hyperpolarizability (β) value ($\beta = 7.14*10^{-30}$ esu) was estimated to be 19 times that of urea ($\beta = 0.3728*10^{-30}$ esu). The band gap energy of the molecule from frontier molecular orbital analysis was determined to be 3.484 eV. The predicted energy gap 3.484 is smaller than the experimentally determined optical band gap energy of 5.45 eV. The second-order hyperpolarizability value through Z-scan procedure ($\gamma = 7.60*10^{-36}$ esu) also showed slight deviation when computed through theoretical analysis ($\gamma = -3.39*10^{-36}$ esu). This is because the theoretical predictions are performed upon an isolated molecule in the gaseous phase, while the experimental value deals with the three-dimensional geometry of the molecule in the solid-state background which is strongly influenced by the crystal field and van der Waals interactions [61].

4 Conclusion

Slow evaporation solution growth technique was employed to form an organic charge transfer complex, 4-dimethylaminopyridinium 3,5-dinitrobenzoate (DMAPDNBA) (Tables 10, 11). The structure and cell parameters have been determined by single crystal and powder X-ray diffraction studies and found to crystallize in non-centrosymmetric orthorhombic crystal system with P212121 as the space group. FTIR analysis helped us to confirm the formation of N–H…O bond between the electron acceptors and donors through the vibrations of different functional groups in the charge transfer complex. UV–visible–NIR spectral study exhibits a wide transparency window from 250 nm to 800 nm with cutoff wavelength 227 nm, band gap energy of 5.45 eV and emission near UV region and finds suitability for non-linear optical transmission systems. The thermogram details reveal the strength of the material to withstand any change in phase transition up to 190 °C and mechanical stability makes the complex a soft material exhibiting reverse indentation size effect. Hence, the material can be exploited for non-linear optical applications. The variations of dielectric constant with the applied frequency and the respective electronic polarizability parameters are discussed in dielectric studies. The laser damage threshold study facilitates the stability of the material when subjected to laser light by a factor of 1.74 GW/cm^2. The SHG signal was found to be eight times that of inorganic KDP and Z-scan study reveals the reverse saturation absorption (RSA) effect and self-focussing nature of the DMAPDNBA complex with an optical limiting threshold of 10.645 J/cm^2 which finds wide application in optoelectronic limiting and switching devices. Additionally, computational analysis employing density functional theory(DFT) and Hartree–Fock theory(HF) strongly confirms the resourceful candidature of the complex in laser-assisted photonic applications by exploiting the calculated hyperpolarizability value (19 times that of the standard urea), reflecting the origin of efficient charge transfer interaction within the molecular system which serves as a key factor in the non-linear optical field.

5 Electronic supplementary material

Supplementary information regarding the molecular structure of DMAPDNBA can be obtained from the electronic paper, Acta Cryst. (2000). C56, e149–e150

Acknowledgements The authors sincerely thank SAIF-IIT Madras for performing single-crystal XRD analysis; Prof. P.K Das, Department of Inorganic chemistry, IISc-Bangalore, for providing laboratory facility to perform SHG measurement and LDT study; VIT-Chennai for microhardness studies; Sacred Heart College, Chennai, for impedance calculation; Mar-Ivanious college, Kerala University, for Z-Scan analysis; Nirmalagiri College, Kerala, and SAT campus, Kannur University, Kerala, for extending help to carry out various characterizations of the synthesized intermediate compound (complex).

References

1. K. Naseema, V. Rao, K.V. Sujith, B. Kalluraya, Curr. Appl. Phys. **10**, 1236 (2010)
2. N.P. Prasad, Photonics and Nonlinear Optics with Molecular Materials and Polymers. Polymer **32**, 1746 (1991)
3. K. Naseema, V. Rao, K.B. Manjunatha, G. Umesh, K.V. Sujith, B. Kalluraya, J. Opt. **39**, 143 (2010). https://doi.org/10.1007/s12596-010-0006-9
4. K. Naseema, S. Ravi, R. Sreedhran, Chinese journal of Physics. **60**, 612 (2019). https://doi.org/10.1016/j.cjph.2019.05.037
5. R.J. Collins, D.F. Nelson, A.L. Schawlow, W. Bond, C.G.B. Garrett, Coherence W. Kaiser, Phys. Rev. Lett. **5**, 303 (1960)
6. J. Pecaut, M. Bagieu-Beucher, Acta Crystallogr. C **49**, 834 (1993)
7. R.S. Mulliken, J. Am. Chem. Soc. **72**, 600 (1950)
8. R.S. Mulliken, W.B. Pearson, *Molecular Complexes* (Wiley Publishers, New York., 1969)
9. J.P. Castaneda, G.S. Denisov, S. Yu Kucherov, V.M. Schreiber, A.V. Shurukhina, J. Mol. Struct. **660**, 25 (2003)
10. S. Manivannan, K. Dhanuskodi, Cryst. Growth Des. **6**, 1285 (2006)

11. P. Srinivasan, T. Kanagasekaran, N. Vijayan, G. Bhagavannarayana, R. Gopalakrishnan, P. Ramasamy, Opt. Mater. **30**, 553 (2007)
12. M. Saravanan, Opt. Mater. **58**, 327 (2016)
13. I.P. Bincy, R. Gopalakrishnan, Opt. Mater. **402**, 22 (2014)
14. J. Johnson, R. Srineevasan, D. Sivavishnu, Materials Science for Energy Technologies. (2019). https://doi.org/10.1016/j.mset.2019.02.001)
15. J. Johnson, R. Srineevasan, D. Sivavishnu, Chemistry Reports. **21**, 20 (2018)
16. J. Johnson, R. Srineevasan, D. Sivavishnu, Physica B: Physics of Condensed Matter (2018). https://doi.org/10.1016/j.physb.2018.03.038
17. M. Rajkumar, M. Saravanabhavan, A. Chandramohan, Opt. Mater. **72**, 247 (2017)
18. P.N. Prasad, Polymer **32**, 1746 (1991)
19. M.L. Carolin, Matter. Lett. **62**, 2245 (2008)
20. M. Amalanathan, Spectrachimica Acta Part A. **78**, 1437 (2011)
21. P.L. Olive, Br. J. Cancer **40**, 83 (1979)
22. P. Srinivasan, T. Kanagasekaran, N. Vijayan, G. Bhagavanarayana, R. Gopalakrishnan, P. Ramasamy, Opt. Mat. **30**, 553 (2007)
23. S. Manivannan, S. Dhanuskodi, Cryst. Growth Des. **4**, 845 (2004)
24. N. Ennaceur, R. Henchiri, B. Jalel, M. Cordier, I. Ledoux-Rak, E. Elaloui, J. of Mol. Structure. **1144**, 25 (2017)
25. R. Henchiri, N. Ennaceur, M. Cordier, I. Ledoux-Rak, E. Elaloui, J. Phys. Chem. Solids **106**, 58 (2017)
26. Hiroyuki Hosomi, Shigeru Ohba, Yoshikatsu Ito, Acta Cryst. **C56**, 149 (2000)
27. S. Stella Mary, S. Shahil Kirupavathy, P. Mythili, P. Srinivasan, T. Kanagasekaran, R. Gopalakrishnan, Spectrochim. Acta, Part A **71**, 10 (2008). https://doi.org/10.1016/j.saa.2007.11.014
28. K.V. Rajendran, D. Jayaraman, R. Jayavel, P. Ramasamy, J. Cryst. Growth **254**, 461 (2003). https://doi.org/10.1016/S0022-0248(03)01097-2
29. T. Uma Devi, N. Lawrence, R. Ramesh Babu, K. Ramamurthi, G. Bhagavannarayana, J. Min. Mater. Character. Eng. **8**, 393 (2009)
30. J. Ramajothi, S. Dhanuskodi, Spectrochim. Acta, Part A **68**, 1213 (2007). https://doi.org/10.1016/j.saa.2007.01.030
31. M.M.A. Jinnah, M. Umadevi, V. Ramakrishnan, J. Raman Spectrosc. **35**, 956 (2004)
32. M. Parthasarathy, R. Gopala Krishnan, Opt. Mat. **35**, 2056 (2013)
33. M.S. Kajamuhideen, K. Sethuraman, K. Ramamurthi, P. Ramasamy, J. Crystal Growth **483**, 16 (2017)
34. I.P. Bincy, R. Gopalakrishnan, J. Cryst. Growth **1**, 1 (2014). https://doi.org/10.1016/j.jcrysgro.2014.03.024
35. J. Dalal, N. Sinha, H. Yadav, B. Kumar, RSC Adv. **5**(71), 57735 (2015)
36. H. Yadav, N. Sinha, B. Kumar, Cryst. Eng. Commun. **16**(46), 10700 (2014)
37. K. Sangwal, Mater. Chem. Phys. **63**(2), 145 (2000)
38. E.M. Onitsch, Mikroskopie. **95**, 12 (1956)
39. M. Hanneman, Metall. Manch. **23**, 135 (1941)
40. K. Sangwal, Mater. Chem. Phys. **63**, 145 (2000)
41. K. Jagannathan, S. Kalainathan, T. Gnanasekaran, Mater. Lett. **61**, 4485 (2007)
42. E.M. Onitsch, Over the microhardness of the metals. Mikroskopie. **2**, 131 (1947)
43. R. Ramesh Babu, K. Sethuraman, N. Vijayan, G. Bhagavannarayana, R. Gopalakrishnan, P. Ramasamy, Cryst. Res. Technol. **41**(9), 906 (2006)
44. S.K. Arora, V. Patel, B. Amin, A. Kothari, Bull. Mater. Sci. **27**, 141 (2004). https://doi.org/10.1016/j.matchemphys.2003.10.017
45. A.M. Badr, H.A. Elshaikh, I.M. Ashraf, J. Eng. Technol. Res. **3**, 62 (2011)
46. K. Boopathi, P. Rajesh, P. Ramasamy, Mater. Res. Bull. **47**(9), 2299 (2012)
47. C. Balarew, R. Duhlew, J. Solid State Chem. **55**, 1 (1984). https://doi.org/10.1016/0022-4596(84)90240-8
48. K.V. Rao, A. Smakula, J. Appl. Phys. **37**, 2031 (1996). https://doi.org/10.1063/1.1714397
49. S.M. Azhar, S.S. Hussaini, M.D. Shirsat, G. Rabbani, M. Shkir, S. Alfaify, H.A. Ghramh, M.I. Baig, M. Anis, Mater. Res. Innovations **1**, 1 (2017). https://doi.org/10.1080/14328917.2017.1392694
50. R. Ragu, M. Akilam, J.P. Angeleena, P.S. LathaMageshwari, S. JeromeDas, J. Mater. Sci.: Mater. Electron. (2017). https://doi.org/10.1007/s10854.019-00933-w
51. P. Karuppasamy, T. Kamalesh, V. Mohankunar, S.A. Kalam, M.S. Pandian, P. Ramasamy, S. Verma, S.V. Rao, J. Mol. Struct. **1**, 1 (2018). https://doi.org/10.1016/j.molstruc.2018.08.074
52. S.K. Kurtz, T.T. Perry, J. App. Phys. **39**, 3798 (1968)
53. G. Wensheng, G. Fang, W. Chunsheng, L. Qitao, Z. Guangyong, W. Dong, S. Zhongshu, J. Sci. China Chem. **45**, 267 (2002)
54. M.S. Bahae, A.A. Said, T.-H. Wei, IEEE J Quant electron. **26**, 760 (1990)
55. P.G.L. Frobel, S.R. Suresh, S. Mayadevi, S. Sreeja, C. Mukherjee, C.I. Muneera, Mater. Chem. Phys. **129**, 981 (2011)
56. Y.-D. Zhang, Z.-Y. Zhao, C.-B. Yao, Opt. Laser Technol. **58**, 207 (2014)
57. M.I. Baig, M. Anis, S. Kalainathan, Mater Technol Adv Perform Mater. **32**, 560 (2017)
58. S.R. Maidur, P.S. Patil, S.V. Rao, AIP Conference Proceeding. **1942**, 100013 (2018). https://doi.org/10.1063/1.5028978
59. CHEMCRAFT, http://www.chemcraftprog.com
60. M. Uthaykumar, A. PricillaJeyakumar, M. Suresh, S. Chandran, G. Vinitha, Mater. Res. Express. **6**, 075102 (2019)
61. V. Kannan, S. Karthick, S. Brahadeeshwaran, Z. Phys. Chem. **1**, 1 (2018). https://doi.org/10.1515/zpch-2018-1231
62. N. Moorthy, P.C. JobePrabakar, S. Ramalingam, S. Periandy, G.V. Pandian, Journal of Theoretical & Computational Science **2**, 1 (2015). https://doi.org/10.4172/2376-130x.1000137